



This is a repository copy of *Effect of deformation twinning on crystallographic texture evolution in a Mg–6.6Zn–0.2Ca (ZX70) alloy during recrystallisation*.

White Rose Research Online URL for this paper:
<http://eprints.whiterose.ac.uk/137068/>

Version: Accepted Version

Article:

Guan, D. orcid.org/0000-0002-3953-2878, Liu, X., Gao, J. et al. (3 more authors) (2019) Effect of deformation twinning on crystallographic texture evolution in a Mg–6.6Zn–0.2Ca (ZX70) alloy during recrystallisation. *Journal of Alloys and Compounds*, 774. pp. 556-564. ISSN 0925-8388

<https://doi.org/10.1016/j.jallcom.2018.10.065>

Article available under the terms of the CC-BY-NC-ND licence (<https://creativecommons.org/licenses/by-nc-nd/4.0/>).

Reuse

This article is distributed under the terms of the Creative Commons Attribution-NonCommercial-NoDerivs (CC BY-NC-ND) licence. This licence only allows you to download this work and share it with others as long as you credit the authors, but you can't change the article in any way or use it commercially. More information and the full terms of the licence here: <https://creativecommons.org/licenses/>

Takedown

If you consider content in White Rose Research Online to be in breach of UK law, please notify us by emailing eprints@whiterose.ac.uk including the URL of the record and the reason for the withdrawal request.



eprints@whiterose.ac.uk
<https://eprints.whiterose.ac.uk/>

Effect of deformation twinning on crystallographic texture evolution in a Mg–6.6Zn–0.2Ca (ZX70) alloy during recrystallisation

Dikai Guan*, Xingguang Liu, Junheng Gao, Le Ma, Brad Wynne, W. Mark Rainforth*

Department of Materials Science and Engineering, University of Sheffield, Sheffield S1 3JD, UK

*Corresponding authors: dikai.guan@sheffield.ac.uk, m.rainforth@sheffield.ac.uk

Abstract

The entire recrystallisation sequence and associated crystallographic texture evolution of Mg-6.6Zn-0.2Ca (ZX70, wt.%) alloy were tracked using a quasi-in-situ electron backscatter diffraction (EBSD) method. The commonly observed grain boundary recrystallisation in conventional Mg alloys was largely restricted, since all the prior grain boundaries were pinned by intermetallic compounds distributed along grain boundaries. A typical “Rare Earth” (RE) texture was observed during the whole recrystallisation process. The RE texture appeared during the nucleation stage because of RE texture orientations introduced by recrystallisation from double twins. This texture was retained during the subsequent grain growth stage because of uniform grain growth. **Recrystallised grains induced by a considerable amount of intermetallic compounds did not change the leading role of double twins on contribution to recrystallised texture.** All results indicate that a small amount of Ca addition into a conventional Mg-Zn alloy system can significantly alter the recrystallised texture from basal texture to RE texture.

Keywords: Magnesium alloy; Recrystallisation; Deformation twins; Texture; Segregation

1. Introduction

A strong basal crystallographic texture is often developed after thermomechanical processing[1-5] giving poor ductility and a strong yield asymmetry in Mg alloys [6, 7]. This texture cannot be effectively modified or eliminated in most conventional Mg alloys [8, 9]. [However, increasing the final rolling temperature in AZ31 largely reduced the recrystallised texture intensity after static recrystallisation\[10, 11\].](#) Recent studies have reported that addition of rare earth (RE) elements can randomise the basal texture by forming characteristic RE textures [1, 6, 12-16]. Various mechanisms and hypotheses have been proposed to explain the formation of RE textures, such as the nucleation sites[2, 4, 6, 13, 14, 17-20], increased non-basal slip activity [5], orientated grain growth [21-25].

RE elements are expensive and strategically important and so there has been much effort to find alternatives. Because of a large atomic radius Ca has attracted substantial attention as a candidate to replace RE elements. Indeed, weakened basal and RE textures have recently been obtained in Ca containing conventional Mg alloys without RE additions [21, 26-36]. The texture modification and RE texture formation were attributed to several different mechanisms: particle stimulating nucleation (PSN)[28, 36], dynamic strain aging[30], preferred growth of oriented nuclei[34], solute drag[21, 33], modification of c/a ratio and stacking fault energy[29, 35]. Zeng et al.[21] systematically compared the texture evolution in Mg-0.1Ca, Mg-0.4Zn and Mg-0.3Zn-0.1Ca (at. %) during static annealing. A weakened texture was only found in the ternary alloy. They hypothesised that co-segregation of Zn and Ca atoms to the grain boundaries in the ternary alloy strongly restricted high-energy GBs mobility of the basal recrystallised grains. They also stated the formation of the weakened texture was attributed to uniform growth of random orientated recrystallised grains originating from grain boundary recrystallisation, rather than shear band recrystallisation or deformation twin

recrystallisation, since there was limited occurrence of both shear bands and deformation twins in the ternary alloy. To further improve the Mg-Zn-Ca alloy strength, one way is to further increase the amount of Zn to enhance solid solution strengthening and age hardening response. There are a number of questions that need addressing: What will happen to texture evolution in a Mg-Zn-Ca alloy with a high amount of Zn if most grain boundaries are decorated by intermetallic compounds and cannot nucleate recrystallised grains? What will be the deformation microstructure, what will be the preferable nucleation sites and can RE texture or weakened basal texture form in Mg-Zn-Ca alloy with high amount of Zn? Which stage of nucleation or grain growth is critical for the final texture formation?

To address these issues, the recrystallisation texture evolution of Mg-6.6Zn-0.2Ca (ZX70) (wt. %) was systematically tracked by a quasi-in-situ EBSD method through the entire recrystallisation sequence. The preferable nucleation sites of grain boundaries reported in the dilute Mg-Zn-Ca alloy[21] were effectively restricted due to second phase particles in this work. Nevertheless, the typical RE texture was still produced in ZX70 due to double twin recrystallisation and uniform grain growth. These results implied Ca played an analogous role to that of RE elements in forming recrystallisation textures during annealing.

2. Experimental procedure

The as-cast Mg-6.6Zn-0.2Ca alloy (ZX70) was supplied by Magnesium Elektron, with chemical compositions listed in Table 1. The alloy was first homogenised at 300 °C for 72h and heated at 350 °C for 8h to avoid incipient melting. Several rectangular plates $50 \times 30 \times 8 \text{ mm}^3$ were then cut from the centre of heat-treated ingot for subsequent cold rolling.

The alloy was cold rolled in one pass to a reduction of 17%. One partly recrystallised and one nearly full recrystallised sample from different parts of this alloy were investigated by EBSD to determine the texture evolution at 300 °C for 720s and 5400s, respectively. Afterwards, another sample from this alloy was scanned by using quasi-in-situ EBSD to fully track the texture evolution in the same area. The quasi-in-situ EBSD data was collected from a large area of about 1.4 mm² from the middle part of ND-RD plane. The EBSD scans were taken from this same area after 135s, 385s, 655s, 1030s, 1630s, 3430s and 7030s annealing at 300 °C. After every EBSD run, the sample was transferred into an argon glove box and sealed in a small aluminium vial. Subsequent annealing was undertaken in a tube furnace with flowing argon with the sample contained in the vial for protection. After annealing, water quenching was undertaken, with the vial providing protection from the water, such that the region of interest on the surface of the sample was protected. To remove any oxide from the surface of interest for next EBSD scan, the annealed sample was given a mild polish using 40 nm OPS suspension. The thickness reduction after this mild polishing was less than 1 µm, measured by a micrometer.

A JEOL 2010F microscope operated at 200 kV was used to conduct high-angle annular dark-field scanning transmission electron microscopy (HAADF-STEM) and energy dispersive X-ray (EDX) spectroscopy analysis. To investigate solute segregation along grain boundaries, a cold-rolled sample was annealed at 300 °C for 5400s. A 3mm disc with the thickness of 100 µm from the middle part of RD-ND plane was produced by traditional grinding. Electropolishing was used to produce a TEM foil sample. To obtain a contamination-free surface after electropolishing, this disc was finally ion milled using a Gatan PIPSII at 0.3 kV for 5 minutes.

3. Results

3.1 Recrystallised grain nucleation and growth

Fig. 1(a) presents a partly recrystallised sample annealed at 300 °C for 720s. Most recrystallised grains were nucleated at deformation twins and intermetallic particles distributed along prior grain boundaries. The recrystallised texture shown in Fig. 1(a) clearly demonstrates RE texture was formed after this partial recrystallisation. Fig. 1(b) gives an EBSD inverse pole figure (IPF) map of another nearly full recrystallised sample from different part of this alloy. Although the origin of the recrystallised grains cannot be identified, a typical RE texture was also produced after nearly full recrystallisation.

To track the recrystallisation behaviour including nucleation, grain growth and corresponding texture evolution during entire recrystallisation process, another sample was subjected to quasi-in-situ EBSD scanning. Fig. 2(a) shows backscattered SEM (BSEM) images of cold-rolled sample for quasi-in-situ EBSD investigation. Significant second phase particles were observed along GBs and in some grains. Fig. 2(b) shows the EBSD IPF map and the corresponding (0002) pole figure is presented in Fig. 2(e). Five orientation peaks were observed in the pole figure of ZX70; the strongest one of 10.0 mud around 41° between RD and TD directions, while the other four with the intensity of 8.8-9.8 mud around 17-27° towards either TD or RD direction. Fig. 2(c) is the corresponding band contrast (BC) image showing that deformation twins can be detected in nearly all deformed grains. To identify twin types, the special boundary component has been superimposed. Additionally, Fig. 2(d) provides the distribution of misorientation angles between neighbouring points in Fig. 2(c). In addition to the low misorientations associated with low angle GBs and noise, there were peaks around 38°, 56° and 86° representing three types of twin boundaries: $\{10\bar{1}2\}$ tension twin (TTW), $\{10\bar{1}1\}$ compression twin (CTW) and $\{10\bar{1}1\}$ - $\{10\bar{1}2\}$ double twin (DTW). The dominant twin boundaries were DTWs. The non-indexed

deformation bands could be either CTWs or DTWs or both. The precise identification needs to be determined by TEM, but TEM results can only provide very local area which cannot represent the whole deformed microstructure. Since CTWs can be immediately transformed to DTWs by secondary tension twinning[37], the non-indexed deformation bands were treated as un-indexed DTWs in this work. This was supported with the different amounts of indexed CTWs and DTWs in Fig. 2 and Figs. 4-5, which showed DTWs were the dominant twin type in the index regions.

No visible recrystallisation took place after annealing 135s in ZX70, which is not presented here. Fig. 3(a-f) records the entire recrystallisation process from nucleation (after annealing 385s) to nearly full recrystallisation (after annealing 7030s) of the same sampling area in Fig. 2(a-c). Apart from preferential nucleation sites of DTWs, another favoured nucleation site in this sample was second phase particles along prior GBs and in some grains. To further make this clear, representative high magnification EBSD images from regions marked by red and yellow rectangles shown in Fig. 2(a) are provided in Figs. 4-5. The unindexed thick dark GBs in Figs. 4-5 correspond to the white second phase particles in Fig. 2(a). The whole region in Fig. 4(a) mainly consists of DTWs, the residual CTWs which have not fully transformed into DTWs, and two sets of TTWs (marked by white arrows) and Fig. 5(a) mainly contained DTWs. During annealing, shown in Figs. 4-5, grains recrystallised quickly from nucleation sites including DTWs, residual CTWs and particles. The recrystallised grains from CTWs could be ignored due to small amount of residual CTWs (Figs. 4-5). However, TTWs shown in Fig. 4(a) did not recrystallise. Some recrystallised grains grew rapidly and expanded into the deformed parent grains as well as TTWs. This static recrystallisation behaviour, especially DTWs recrystallisation, was exactly the same as that which occurred in the RE containing WE43 alloy[20]. The highlighted grains in Fig. 4(h) was originally from PSN at the prior GBs and the volume fraction is only 13.8%. Fig. 6(a) provides the (0002) pole figure of all recrystallised grains

in Fig. 4(h) and Fig. 6(b) gives the (0002) pole figure of recrystallised grains excluding highlighted grains in Fig. 4(h). Comparing these, the texture intensity slightly decreased from 11.5mud to 10.0mud but the position of the texture components did not change (Fig. 6). [Similar results which were not provided here were found in Fig. 5](#). Therefore, although the amount of intermetallic compounds was considerable in this alloy, recrystallised grains introduced by particle stimulated nucleation (PSN) did not change the leading role of DTWs on contribution to recrystallised texture.

3.2 Recrystallised texture evolution

Fig. 7(a-f) are (0002) pole figures using data collected only from recrystallised areas in Fig. 3(a-f). The morphology of RE texture was already initiated during the nucleation dominated stage, as shown in Fig. 7(a-b) after annealing at 385s and 655s. During subsequent annealing where recrystallised grain growth dominated, the RE texture components around 35° towards TD directions gradually strengthened while the texture component around basal texture reduced in terms of intensity and area after annealing from 1030s to 7030s (Fig. 7(c-f)). The texture positions were quite different from the corresponding cold-rolled texture shown in Fig. 2(e).

To find out the reason why the basal texture component weakened during the grain growth stage, the corresponding EBSD data within this texture component in the same area in (0002) pole figures were extracted (a red rectangle marked in Fig. 7(c-f)). Fig. 8 shows the corresponding collected quasi-in-situ EBSD data from the red rectangle areas shown in Fig. 7. Overall, the volume fraction of this basal texture components in the area that had fully recrystallised (V_r), excluding the residual deformed area, decreased with annealing. The texture shape and position did not change significantly. After annealing to 1030s, 1630s, 3430s and 7030s, the average grain size of all recrystallised grains in this

sample was 7.5 μm , 9.1 μm , 13.8 μm and 16.2 μm , while the average grain size of weakened texture component in Fig. 8 was 7.2 μm , 9.0 μm , 12.9 μm and 15.5 μm .

Fig. 9(a) provides the distribution of $\langle 0001 \rangle$ direction corresponding to each grain orientation of the cold-rolled sample shown in Fig. (2). Two main peaks positioned at 17.5° and 42.5° away from ND were detected. After annealing, the texture component in the range of $70\text{-}90^\circ$ was increased and the peak texture component moved to $25\text{-}45^\circ$ tilting away from ND. The peak relative frequency decreased from ~ 0.055 after cold rolling to ~ 0.030 after sequential annealing process.

To explore whether grains with specific orientations grow preferentially during annealing, the recrystallised grains were divided into four groups based on the angle differences between their c-axis and $\langle 0001 \rangle$ basal texture (the tilt of basal poles away from ND). These four groups were $0\text{-}20^\circ$, $20\text{-}45^\circ$, $45\text{-}70^\circ$ and $70\text{-}90^\circ$ tilted away from the ND and were designated as texture component A (TCA), texture component B (TCB), texture component C (TCC) and texture component D (TCD) in the following sections. Fig. 10 shows the average grain size of the recrystallised grains of each texture component. In general, the difference in average grain size of each texture component was negligible.

Fig. 11 gives the volume fraction of the individual recrystallised texture components based on total recrystallised area. The volume fraction of each texture component was stable between 385s and 1630s annealing intervals. Afterwards, the volume fraction of TCB and TCC fluctuated, TCA kept decreasing while TCD was not changed after annealing for 3430s and 7030s. Combining the results of Fig. 10 and Fig. 11, it can be concluded that there was no orientated grain growth during recrystallisation.

3.3 Concurrent precipitation and solute segregation during recrystallisation

Fig. 12 provides a BSEM image of a sample after annealing at 300 °C for 300s. Precipitates were distributed along twin boundaries as well as prior GBs (see red arrows). This concurrent precipitation during recrystallisation was also reported in previous in-situ TEM studies [38].

Fig. 13(a-b) shows a typical BF and corresponding HAADF-STEM images from a sample after annealing at 300 °C for 5400s. Fig. 13(c-d) presents the EDX line scan results across the grain boundary. The results indicated Zn and Ca co-segregated along this grain boundary.

4. Discussion

In conventional Mg alloys, TTWs are the dominant twin type in hard orientated grains for basal slip owing to a low critical resolved shear stress (CRSS) and high Schmid factor for tension twinning. However, in this study DTWs that had rapidly transformed from CTWs were the main deformation mechanism in both alloys. A high frequency of CTWs and DTWs has also been observed in other Ca containing alloys, such as the binary Mg-Ca alloys ZX11, reported by Lee et al. [29, 35] and ZX31 reported by Kim et al.[34], respectively.

In this work, the preferential nucleation sites were DTWs (Fig. 1 and Figs. 3-5), and the additional nucleation at coarse second phase particles. As shown in Fig. 4(g-h) and Fig. 6, the proportion of recrystallised grains from PSN was not enough to change the dominant role of DTWs on the recrystallised texture [in this large deformed grain](#). CTWs and DTWs have been reported to nucleate recrystallised grains with RE orientations [12, 39, 40], which was experimentally confirmed in our previous studies [13, 20]. [Although TTW related recrystallisation was reported during dynamic recrystallisation](#) [41], TTWs were not effective nucleation sites due to minimal accumulation of dislocations and consequently low elastic strain energy along mobile twin boundaries [13, 20]. Moreover, the grain boundary recrystallisation reported in [21] was restricted by pre-existing second phase particles along prior grain boundaries and was further retarded by concurrent precipitation along

grain boundaries during recrystallisation. Therefore, the RE texture produced during nucleation stages in this alloy can be mainly attributed to DTWs recrystallisation.

After close examination of quasi-in-situ EBSD scans, the volume of each recrystallised texture component did not change significantly. TCA texture component close to basal orientations decreased while TCB fluctuated and TCC and TCD slightly increased through the entire annealing process (Fig. 11). Obvious concomitant precipitation took place before 300s annealing (Fig. 12). The similar average grain size (Fig. 10) and relatively stable volume fraction of all four texture components (Fig. 11) during the entire nucleation and early grain growth stages can be attributed to the synergic effect of solute drag and particle pinning. In addition, the precipitates along prior grain boundaries could also further reduce the occurrences of recrystallisation along grain boundaries.

The texture position and intensity before and after recrystallisation were altered by static recrystallisation, Fig. 9. Overall, the recrystallised texture component distribution was preserved during the whole recrystallisation process. Nevertheless, changes in local distribution need to be noted. For instance, the volume fraction of texture component containing 0-10° tilted away from the ND decreased (marked by black boxes in Fig. 9) and the peak texture components (marked by blue boxes in Fig. 9) slightly increased during annealing in both alloys, which is consistent with the (0002) pole figure results in Figs. 7-8. Because the grain orientation distribution in large sampling areas shown in Fig. 1, Fig. 3 and Fig. 8 was uniform, the decreased grain growth of uniformly distributed basal grains in these sampled areas could not be attributed to the different positions in local areas. All the results presented in Figs. 7-9 confirmed the synergistic effect of solute drag and

particle pinning on basal grain growth was more prominent than on non-basal grains, which made most small basal grains lose their growth advantage when they meet relatively large grains with other orientations.

From the results of this study, the typical RE textures were formed during the nucleation stage of static recrystallisation. The RE orientated grains survived and dominated the texture evolution. This was because recrystallisation from other sources (e.g., grain boundaries) was retarded due to solute drag and particle pinning from concurrent precipitation, which preserved the RE texture introduced by DTW recrystallisation during the entire annealing process. These results suggest that Ca acted in a similar manner to RE elements during annealing: imparting solute drag, concurrent precipitation, restricting preferable growth of basal grains. The results also implied the preferable nucleation sites played a critical role in forming the final RE texture. In this work, the DTWs were shown to be effective nucleation sites for producing RE texture while new orientations introduced by PSN made negligible contribution for RE texture formation. Therefore, in order to manipulate the recrystallised texture of Mg alloys, the choices of deformation microstructures and corresponding preferable nucleation sites need to be considered when designing the composition and thermomechanical process of Mg alloys.

5. Conclusions

RE texture was formed after cold rolling and subsequent annealing in all three samples from different areas of this alloy. The entire recrystallisation sequence of this alloy was examined using the quasi-in-situ EBSD method during annealing, and the following conclusions can be drawn:

- (1) Grain boundary recrystallisation was largely restricted by the pre-existing second phase particles distributed along grain boundaries

- (2) Zn and Ca co-segregation occurred along grain boundaries. Concurrent precipitation occurred from the early stage of recrystallisation. Precipitates were preferentially distributed along the prior grain and twin boundaries.
- (3) DTWs were the dominate nucleation sites and contributed mainly to the final recrystallised textures. **Although the amount of intermetallic compounds was considerable in this alloy, recrystallised grains introduced by particle stimulated nucleation did not alter the leading role of DTWs on recrystallised texture.**
- (4) Characteristic RE textures were produced and preserved by uniform grain growth during the whole recrystallisation sequence due to synergic effects of solute drag and particle pinning introduced by concurrent precipitation.
- (5) These results suggest that Ca played a similar role to that of RE elements in controlling recrystallisation texture. However, changes in local distribution need to be noted: the RE texture components were enhanced while the texture around basal orientations weakened gradually during annealing. Nevertheless, these local changes did not alter the RE texture morphologies in both alloys.

Acknowledgments

This work was funded by the EPSRC DARE Project, EP/L025213/1.

References

- [1] A. Imandoust, C.D. Barrett, T. Al-Samman, K.A. Inal, H. El Kadiri, A review on the effect of rare-earth elements on texture evolution during processing of magnesium alloys, *J. Mater. Sci.* (2016) 1-29.
- [2] T. Al-Samman, X. Li, Sheet texture modification in magnesium-based alloys by selective rare earth alloying, *Mater. Sci. Eng. A* 528 (2011) 3809-3822.
- [3] J. Hirsch, T. Al-Samman, Superior light metals by texture engineering: Optimized aluminum and magnesium alloys for automotive applications, *Acta Mater.* 61 (2013) 818-843.
- [4] I. Basu, T. Al-Samman, G. Gottstein, Shear band-related recrystallization and grain growth in two rolled magnesium-rare earth alloys, *Mater. Sci. Eng. A* 579 (2013) 50-56.

- [5] S. Sandlöbes, S. Zaefferer, I. Schestakow, S. Yi, R. Gonzalez-Martinez, On the role of non-basal deformation mechanisms for the ductility of Mg and Mg–Y alloys, *Acta Mater.* 59 (2011) 429-439.
- [6] E.A. Ball, P.B. Prangnell, Tensile-compressive yield asymmetries in high strength wrought magnesium alloys, *Scripta Metallurgica et Materialia* 31 (1994) 111-116.
- [7] M.R. Barnett, Twinning and the ductility of magnesium alloys: Part I: “Tension” twins, *Mater. Sci. Eng. A* 464 (2007) 1-7.
- [8] J.J. Bhattacharyya, S.R. Agnew, G. Muralidharan, Texture enhancement during grain growth of magnesium alloy AZ31B, *Acta Mater.* 86 (2015) 80-94.
- [9] M.A. Steiner, J.J. Bhattacharyya, S.R. Agnew, The origin and enhancement of texture during heat treatment of rolled AZ31B magnesium alloys, *Acta Mater.* 95 (2015) 443-455.
- [10] X. Huang, K. Suzuki, Y. Chino, M. Mabuchi, Improvement of stretch formability of Mg–3Al–1Zn alloy sheet by high temperature rolling at finishing pass, *J. Alloys Compd.* 509 (2011) 7579-7584.
- [11] X. Huang, K. Suzuki, Y. Chino, M. Mabuchi, Influence of rolling temperature on static recrystallization behavior of AZ31 magnesium alloy, *J. Mater. Sci.* 47 (2012) 4561-4567.
- [12] D. Griffiths, Explaining texture weakening and improved formability in magnesium rare earth alloys, *Mater. Sci. Technol.* 31 (2015) 10-24.
- [13] D. Guan, W.M. Rainforth, L. Ma, B. Wynne, J. Gao, Twin recrystallization mechanisms and exceptional contribution to texture evolution during annealing in a magnesium alloy, *Acta Mater.* 126 (2017) 132-144.
- [14] N. Stanford, M.R. Barnett, The origin of “rare earth” texture development in extruded Mg-based alloys and its effect on tensile ductility, *Mater. Sci. Eng. A* 496 (2008) 399-408.
- [15] N. Stanford, D. Atwell, A. Beer, C. Davies, M.R. Barnett, Effect of microalloying with rare-earth elements on the texture of extruded magnesium-based alloys, *Scr. Mater.* 59 (2008) 772-775.
- [16] M. Sanjari, A. Farzadfar, A.S.H. Kabir, H. Utsunomiya, I.-H. Jung, R. Petrov, L. Kestens, S. Yue, Promotion of texture weakening in magnesium by alloying and thermomechanical processing: (I) alloying, *J. Mater. Sci.* 49 (2014) 1408-1425.
- [17] J.D. Robson, D.T. Henry, B. Davis, Particle effects on recrystallization in magnesium–manganese alloys: Particle-stimulated nucleation, *Acta Mater.* 57 (2009) 2739-2747.
- [18] I. Basu, T. Al-Samman, Twin recrystallization mechanisms in magnesium-rare earth alloys, *Acta Mater.* 96 (2015) 111-132.
- [19] P. Hidalgo-Manrique, S.B. Yi, J. Bohlen, D. Letzig, M.T. Pérez-Prado, Effect of Nd Additions on Extrusion Texture Development and on Slip Activity in a Mg-Mn Alloy, *Metall. Mater. Trans. A* 44 (2013) 4819-4829.
- [20] D. Guan, W.M. Rainforth, J. Gao, J. Sharp, B. Wynne, L. Ma, Individual effect of recrystallisation nucleation sites on texture weakening in a magnesium alloy: Part 1- double twins, *Acta Mater.* 135 (2017) 14-24.
- [21] Z.R. Zeng, Y.M. Zhu, S.W. Xu, M.Z. Bian, C.H.J. Davies, N. Birbilis, J.F. Nie, Texture evolution during static recrystallization of cold-rolled magnesium alloys, *Acta Mater.* 105 (2016) 479-494.
- [22] J. Robson, Effect of Rare-Earth Additions on the Texture of Wrought Magnesium Alloys: The Role of Grain Boundary Segregation, *Metall. Mater. Trans. A* 45 (2014) 3205-3212.
- [23] I. Basu, T. Al-Samman, Triggering rare earth texture modification in magnesium alloys by addition of zinc and zirconium, *Acta Mater.* 67 (2014) 116-133.

- [24] J.D. Robson, S.J. Haigh, B. Davis, D. Griffiths, Grain Boundary Segregation of Rare-Earth Elements in Magnesium Alloys, *Metall. Mater. Trans. A* 47 (2016) 522-530.
- [25] I. Basu, K.G. Pradeep, C. Mießen, L.A. Barrales-Mora, T. Al-Samman, The role of atomic scale segregation in designing highly ductile magnesium alloys, *Acta Mater.* 116 (2016) 77-94.
- [26] Y.Z. Du, X.G. Qiao, M.Y. Zheng, D.B. Wang, K. Wu, I.S. Golovin, Effect of microalloying with Ca on the microstructure and mechanical properties of Mg-6 mass%Zn alloys, *Materials & Design* 98 (2016) 285-293.
- [27] M.G. Jiang, C. Xu, T. Nakata, H. Yan, R.S. Chen, S. Kamado, Development of dilute Mg-Zn-Ca-Mn alloy with high performance via extrusion, *J. Alloys Compd.* 668 (2016) 13-21.
- [28] B. Zhang, Y. Wang, L. Geng, C. Lu, Effects of calcium on texture and mechanical properties of hot-extruded Mg-Zn-Ca alloys, *Mater. Sci. Eng. A* 539 (2012) 56-60.
- [29] J.-Y. Lee, Y.-S. Yun, B.-C. Suh, N.-J. Kim, W.-T. Kim, D.-H. Kim, Comparison of static recrystallization behavior in hot rolled Mg-3Al-1Zn and Mg-3Zn-0.5Ca sheets, *J. Alloys Compd.* 589 (2014) 240-246.
- [30] T. Wang, L. Jiang, R.K. Mishra, J.J. Jonas, Effect of Ca Addition on the Intensity of the Rare Earth Texture Component in Extruded Magnesium Alloys, *Metall. Mater. Trans. A* 45 (2014) 4698-4709.
- [31] H. Ding, X. Shi, Y. Wang, G. Cheng, S. Kamado, Texture weakening and ductility variation of Mg-2Zn alloy with CA or RE addition, *Mater. Sci. Eng. A* 645 (2015) 196-204.
- [32] J. Bohlen, J. Wendt, M. Nienaber, K.U. Kainer, L. Stutz, D. Letzig, Calcium and zirconium as texture modifiers during rolling and annealing of magnesium-zinc alloys, *Mater. Charact.* 101 (2015) 144-152.
- [33] N. Stanford, The effect of calcium on the texture, microstructure and mechanical properties of extruded Mg-Mn-Ca alloys, *Mater. Sci. Eng. A* 528 (2010) 314-322.
- [34] D.W. Kim, B.C. Suh, M.S. Shim, J.H. Bae, D.H. Kim, N.J. Kim, Texture Evolution in Mg-Zn-Ca Alloy Sheets, *Metall. Mater. Trans. A* 44 (2013) 2950-2961.
- [35] J.-Y. Lee, Y.-S. Yun, W.-T. Kim, D.-H. Kim, Twinning and texture evolution in binary Mg-Ca and Mg-Zn alloys, *Met. Mater. Int.* 20 (2014) 885-891.
- [36] H. Pan, Y. Ren, H. Fu, H. Zhao, L. Wang, X. Meng, G. Qin, Recent developments in rare-earth free wrought magnesium alloys having high strength: A review, *J. Alloys Compd.* 663 (2016) 321-331.
- [37] S. Niknejad, S. Esmaeili, N.Y. Zhou, The role of double twinning on transgranular fracture in magnesium AZ61 in a localized stress field, *Acta Mater.* 102 (2016) 1-16.
- [38] D. Guan, J. Nutter, J. Sharp, J. Gao, W. Mark Rainforth, Direct observation of precipitation along twin boundaries and dissolution in a magnesium alloy annealing at high temperature, *Scr. Mater.* 138 (2017) 39-43.
- [39] S.A. Farzadfar, É. Martin, M. Sanjari, E. Essadiqi, S. Yue, Texture weakening and static recrystallization in rolled Mg-2.9Y and Mg-2.9Zn solid solution alloys, *J. Mater. Sci.* 47 (2012) 5488-5500.
- [40] K. Hantzsche, J. Bohlen, J. Wendt, K.U. Kainer, S.B. Yi, D. Letzig, Effect of rare earth additions on microstructure and texture development of magnesium alloy sheets, *Scr. Mater.* 63 (2010) 725-730.
- [41] A.G. Beer, M.R. Barnett, Microstructural Development during Hot Working of Mg-3Al-1Zn, *Metall. Mater. Trans. A* 38 (2007) 1856-1867.

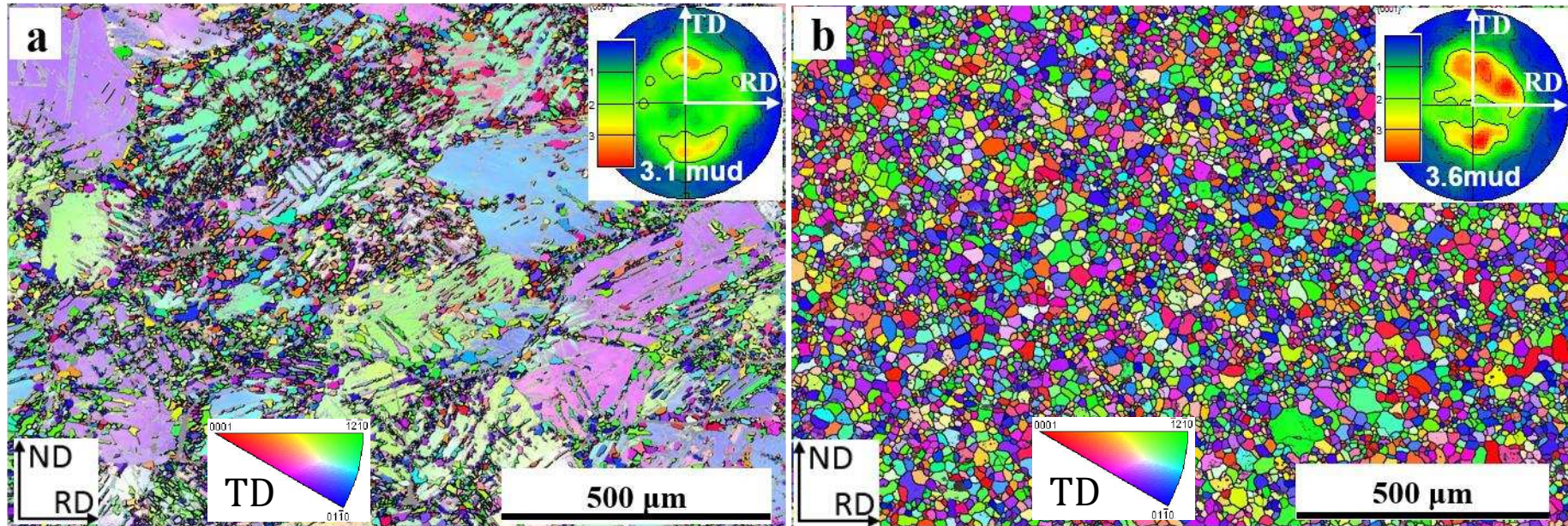


Figure 1 (a) EBSD IPF image of a cold-rolled sample after annealing at 300 °C for 720s, (b) EBSD IPF image of another cold-rolled sample after annealing at 300 °C for 5400s. The insets are corresponding (0002) pole figures. Observation along TD was applied to IPF triangle.

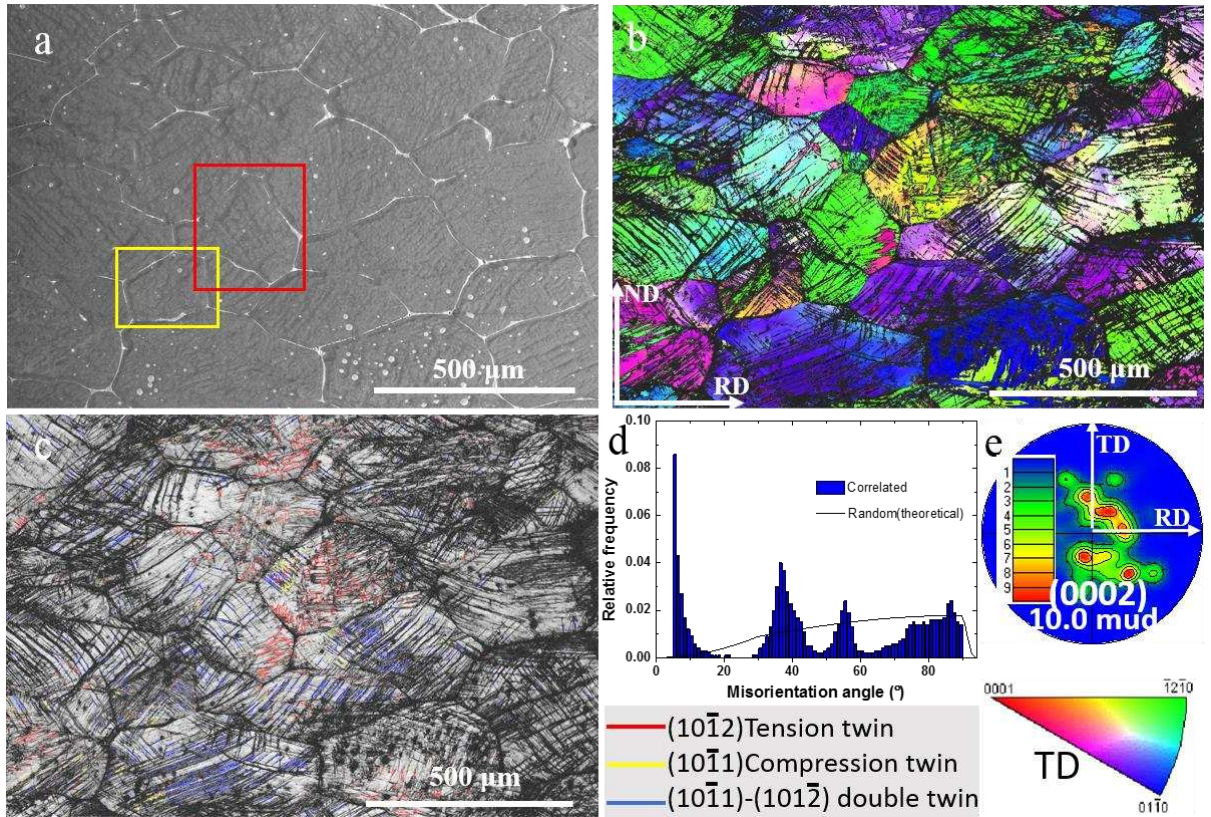


Figure 2 (a) BSEM image of cold-rolled sample, (b) corresponding EBSD IPF image, (c) band contrast (BC) map superimposed by various twin boundaries, (d) misorientation angle and (e) (0002) pole figure of (b). Observation along TD was applied to IPF triangle.

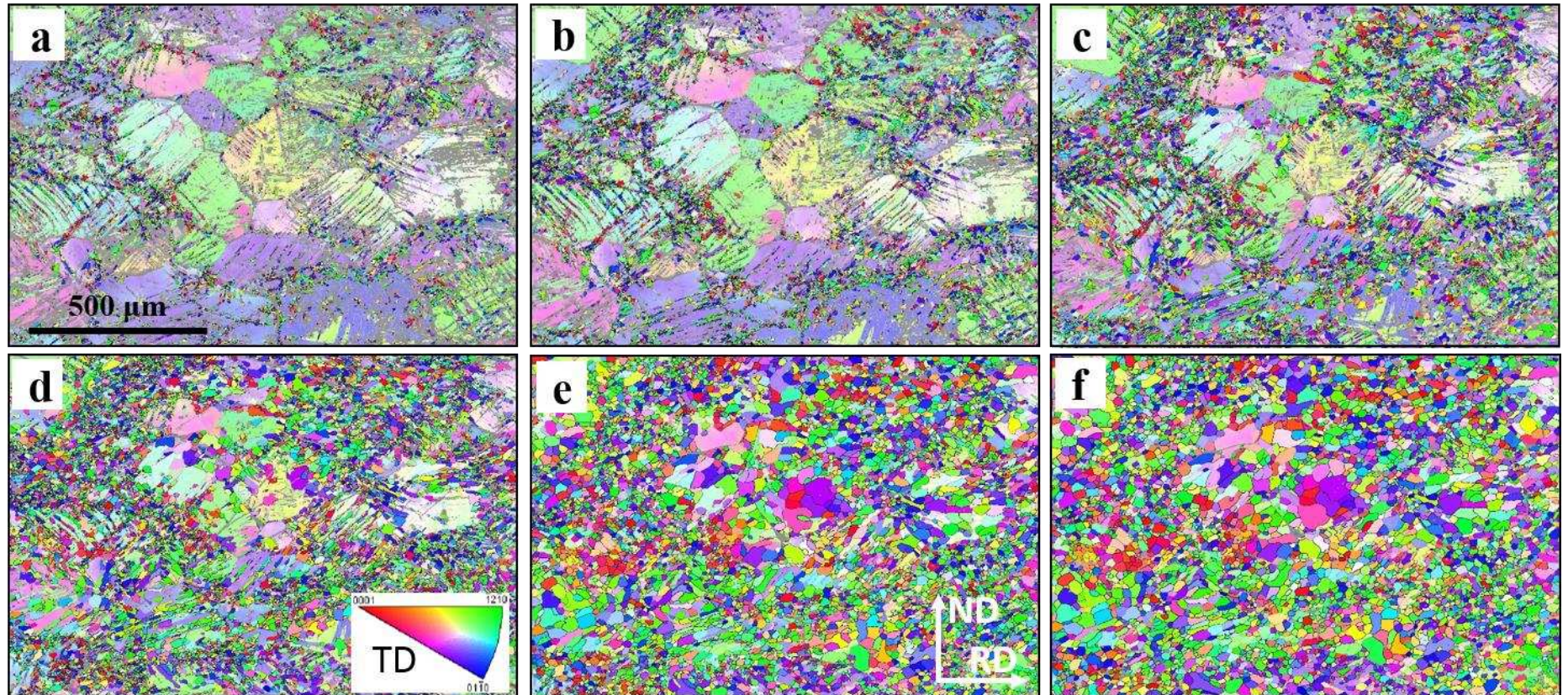


Figure 3 (a) EBSD IPF maps of cold-rolled sample only showing recrystallised at annealing intervals of (a) 385s, (b) 655s, (c) 1030s, (d) 1630s, (e) 3430s, and (f) 7030s. Observation along TD was applied to IPF triangle.

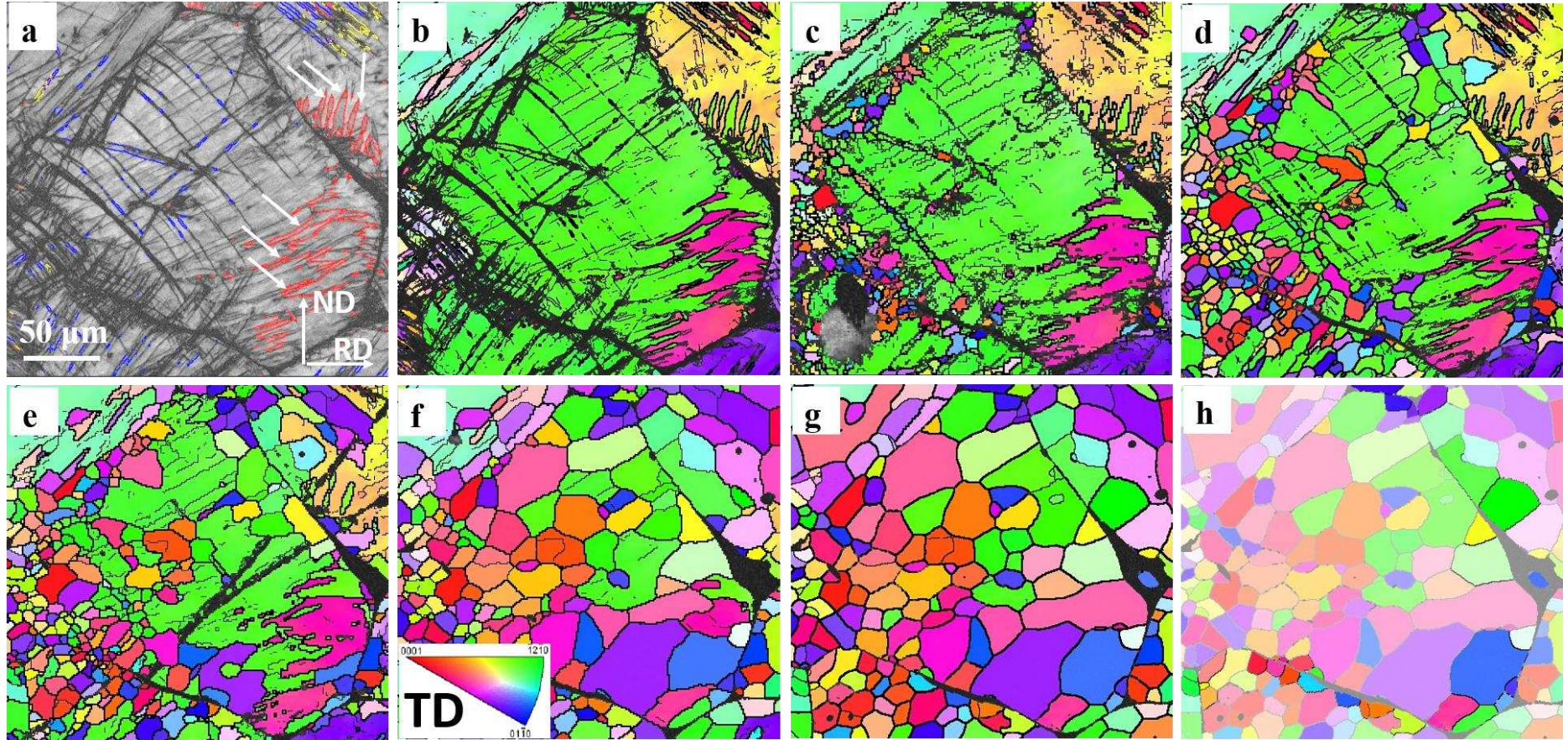


Figure 4 Quasi-in-situ EBSD IPF maps presenting recrystallised grain nucleation and growth (a) cold-rolled sample, band contrast (BC) map superimposed by various twin boundaries (see twin boundary type colour codes in Fig. 2), (b) corresponding cold-rolled sample EBSD IPF images and at annealing intervals of (c) 385s, (d) 1030s, (e) 1630s, (f) 3430s and (g) 7030s, (h) highlighted PSN grains originated from second phase particles along prior grain boundaries in (g). Observation along TD was applied to IPF triangle.

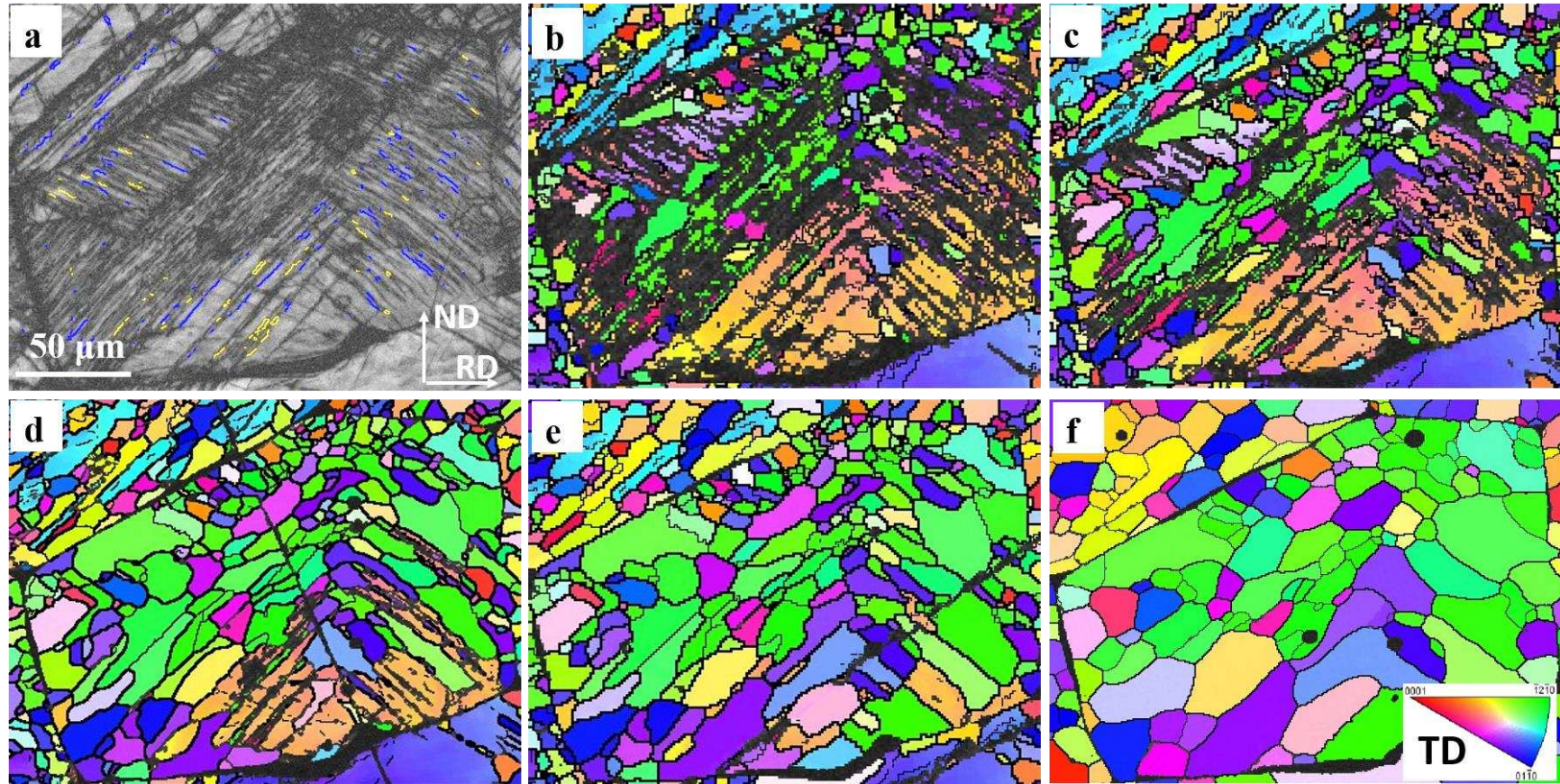


Figure 5 Quasi-in-situ EBSD IPF maps presenting recrystallised grain nucleation and growth (a) cold-rolled sample:band contrast (BC) map superimposed by various twin boundaries (see twin boundary types in Fig. 2), and corresponding EBSD IPF images at annealing intervals of (b) 385s, (c) 1030s, (d) 1630s, (e) 3430s, and (f) 7030s. Observation along TD was applied to IPF triangle.

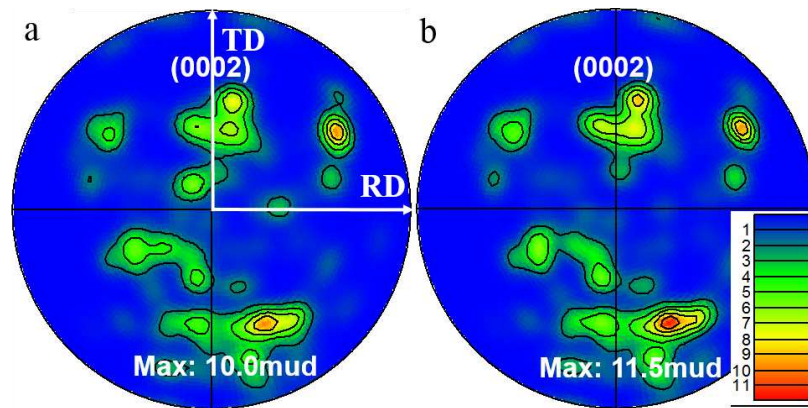


Figure 6 (0002) pole figures consisting (a) all recrystallised grains in Fig. 4(h), and (b) recrystallised grains excluding highlighted grains in Fig. 4(h).

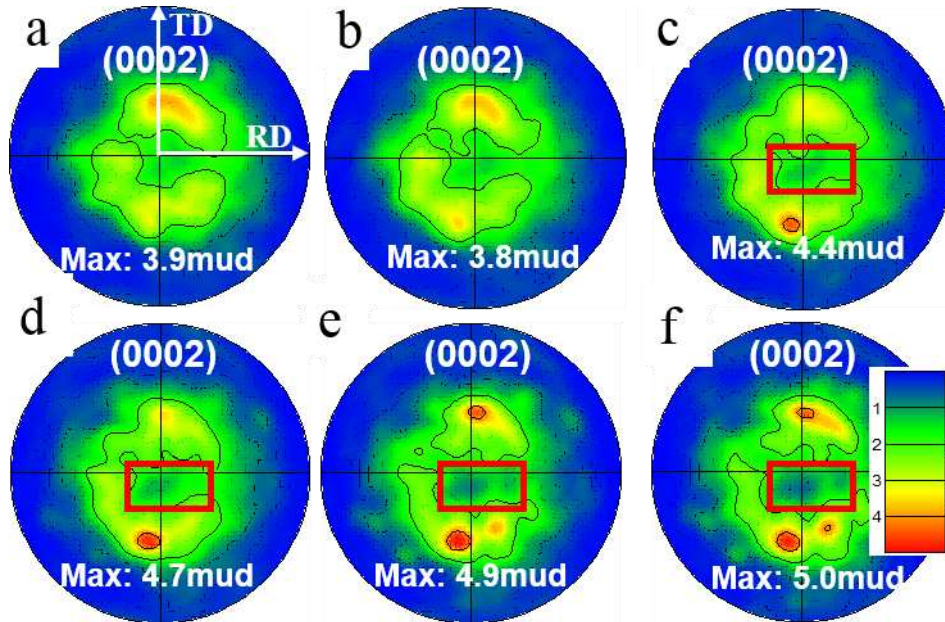


Figure 7 (0002) pole figures consisting only of recrystallised grains at annealing intervals of (a) 385s, (b) 655s, (c) 1030s, (d) 1630s, (e) 3430s, and (f) 7030s.

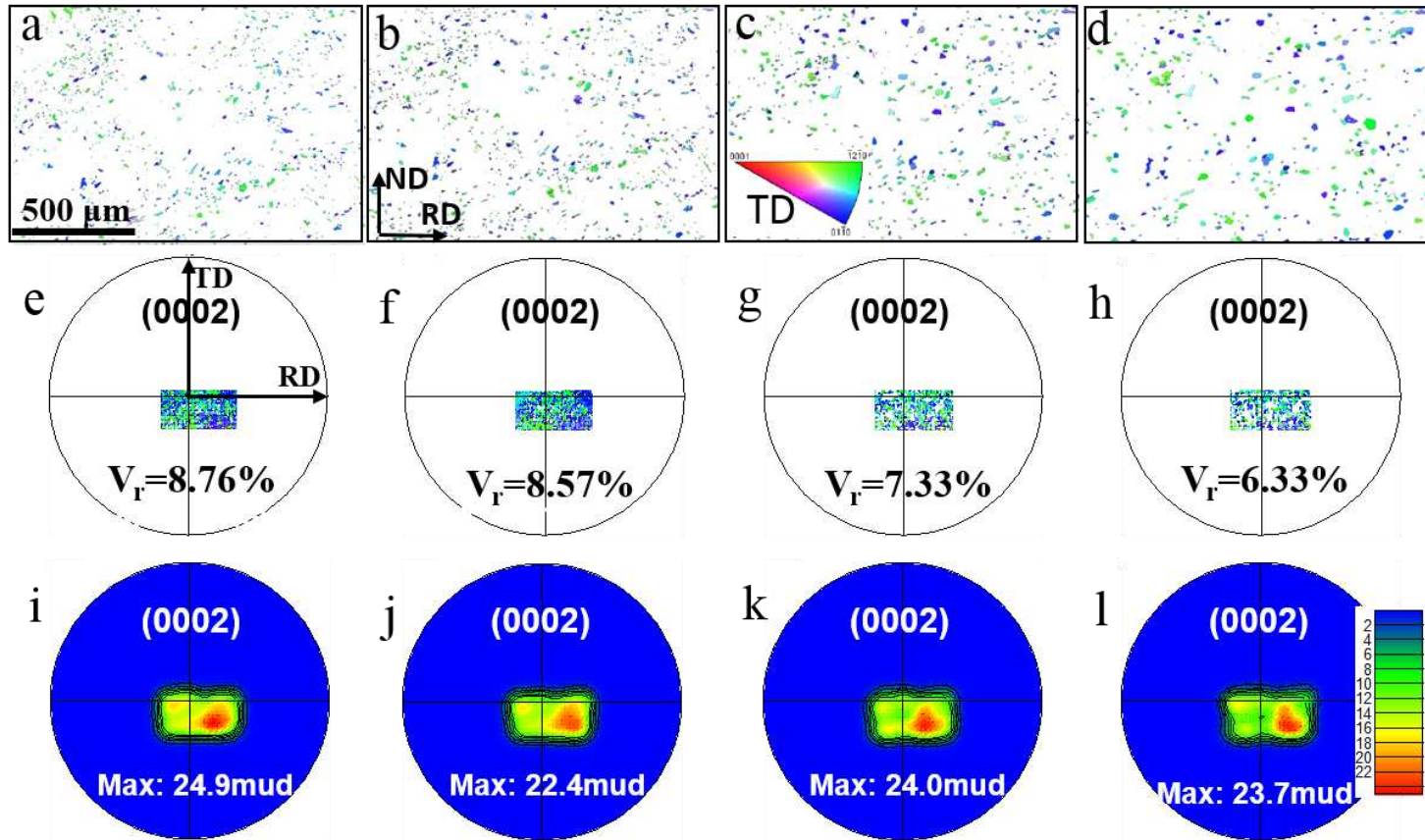


Figure 8 Quasi-in-situ EBSD IPF maps presenting recrystallised grains within the same area marked by red box in Fig. 7 at annealing intervals of (a) 1030s, (b) 1630s, (c) 3430s, and (d) 7030s. (e-h) are corresponding (0002) scattered point pole figure and (i-l) are corresponding recalculated contour (0002) pole figure. Observation along TD was applied to IPF triangle.

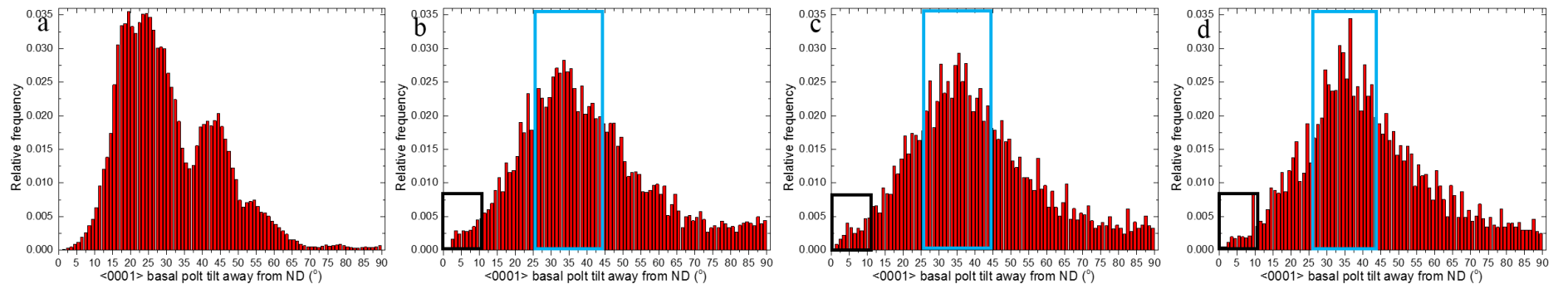


Figure 9 $\langle 0001 \rangle$ basal texture tilted away from Normal Direction (ND) at annealing intervals of (a) 0s, (b) 385s, (c) 1030s, and (d)

3430s.

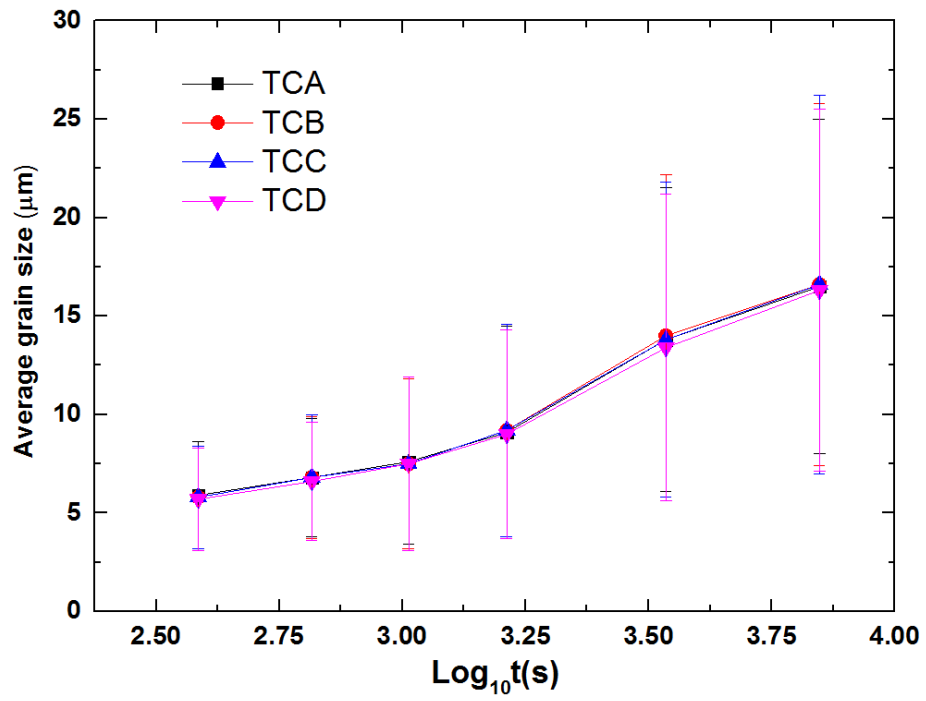


Figure 10 Average grain size of each recrystallised texture component as a function of annealing time.

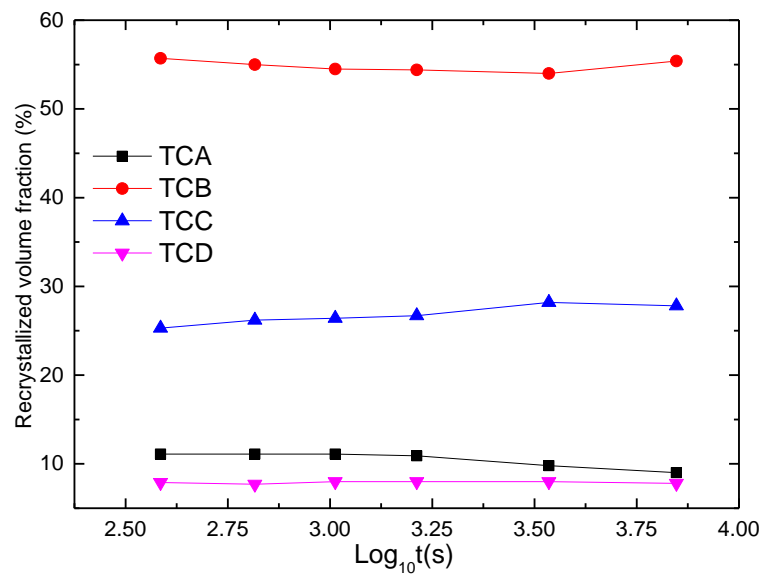


Figure 11 Recrystallised volume fraction of each texture component based only on the recrystallised area as a function of annealing time.

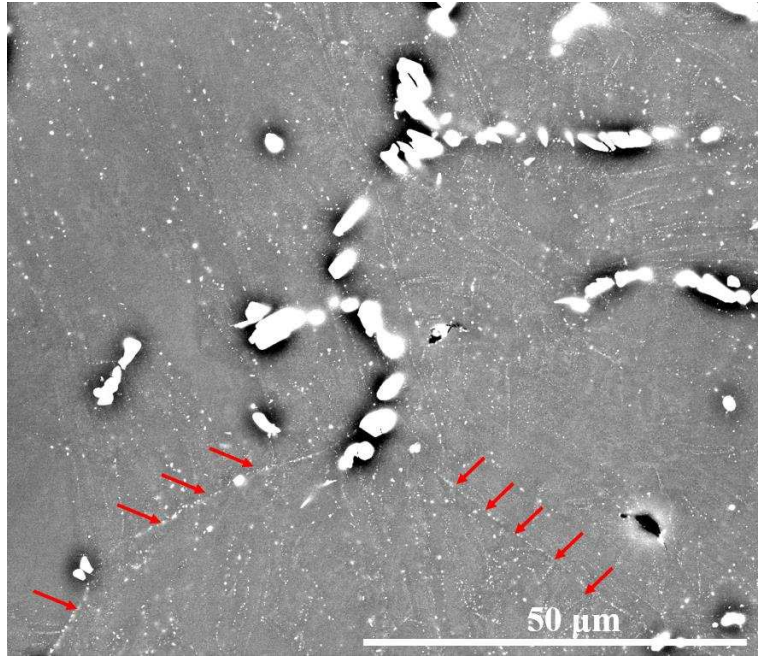


Figure 12 BSEM image from cold-rolled sample after annealing at 300 °C for 300s.

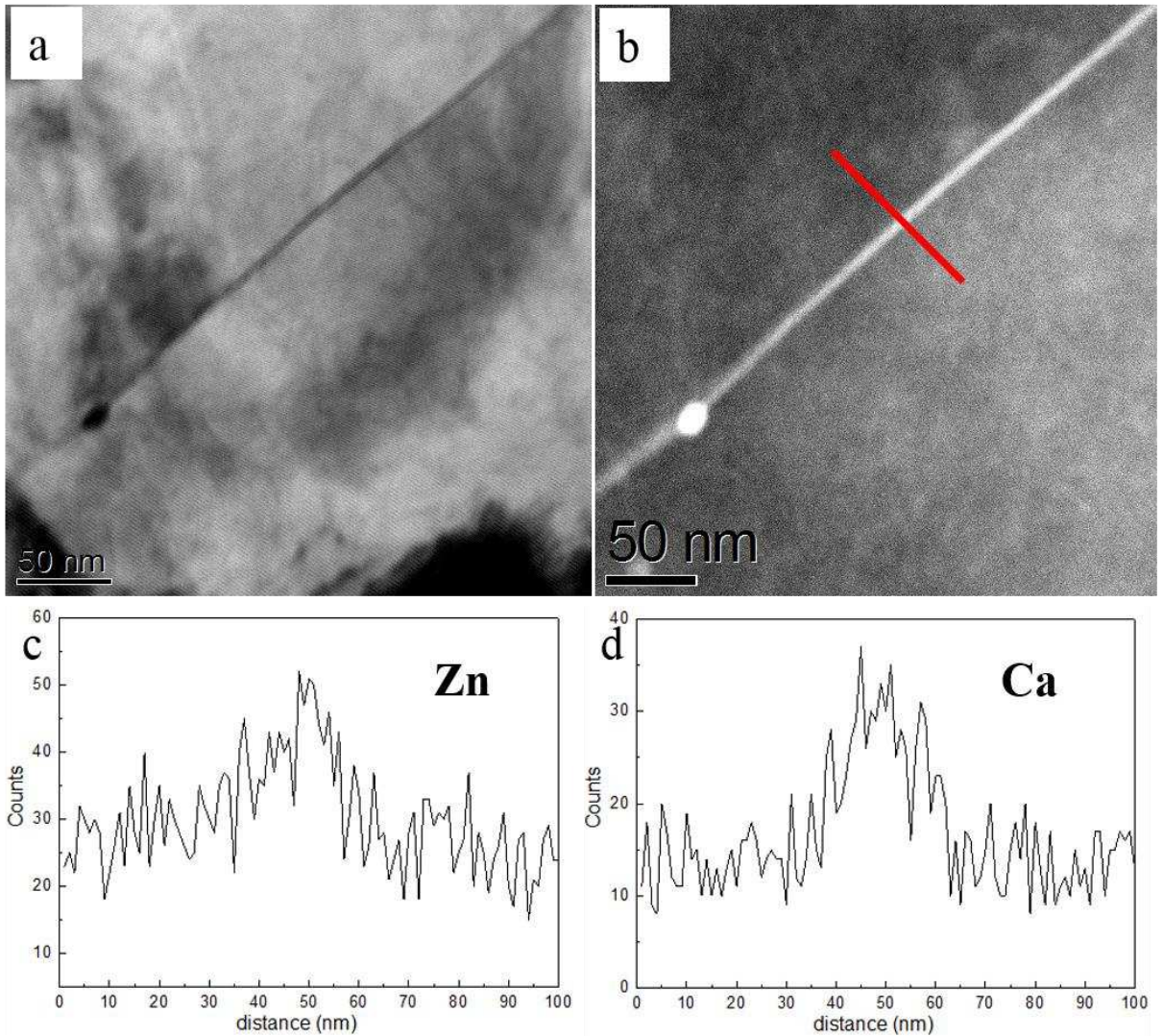


Figure 13 (a) A typical BF-STEM image and (b) corresponding HAADF-STEM image from a cold-rolled sample after annealing at 300 °C for 5400s, EDX line scan showing (c) Zn solute segregation (d) Ca solute segregation.